complex visibility measured in the (u,v) plane sampled by the ALMA observations of N_2H^+.

As demonstrated in Fig. 2A, the inner radius is well constrained to 28 to 31 AU (3σ). This edge determination was aided by the nearly face-on viewing geometry because this minimizes the impact of the detailed vertical structure on the disk-modeling outcome. Furthermore, the Keplerian kinematics of the gas help to constrain the size scale at a level finer than the spatial resolution implied by the synthesized beam size. As a result, the fitted inner radius is robust to the details of the density and temperature model (table S2) (*20*). In the context of this model, the best-fit N_2H^+ inner radius corresponds to a CO midplane snow line at a temperature of 17 K. The best-fit N_2H^+ column density profile is presented in Fig. 2B together with the best-fit ^{13}CO profile, assuming a CO freeze-out temperature of 17 K (*20*) (fig. S5 and table S3). We fit ^{13}CO emission [obtained with the Submillimeter Array (*20*)] because the main isotopologue CO lines are optically thick. The N_2H^+ column density contrast across the CO snow line is at least an order of magnitude (*20*). Simulated ALMA observations of the best-fit N_2H^+ $J = 4–3$ model are shown in Fig. 2C, demonstrating the excellent agreement.

Our quantitative analysis thus confirms the predictions that N_2H^+ traces the snow line of the abundant volatile, CO. Furthermore, the agreement between the quantitative analysis and the visual estimate of the N_2H^+ inner radius demonstrates that N_2H^+ imaging is a powerful tool to determine the CO snow line radii in disks, whose density and temperature structures have not been modeled in detail. N_2H^+ imaging with ALMA may therefore be used to provide statistics on how snow line locations depend on parameters of interest for planet formation theory, such as the evolutionary stage of the disks.

The locations of snow lines in solar nebula analogs such as TW Hya are also important to understand the formation dynamics of the solar system. The H_2O snow line is key to the formation of Jupiter and Saturn (*29*), whereas CH_4 and CO freeze-out enhanced the solid surface density further out in the solar nebula, which may have contributed to the feeding zones of Uranus and Neptune (*30*), depending on exactly where these ice giants formed. In the popular Nice model for the dynamics of the young solar system, Uranus formed at the largest radius of all planets, at ~17 AU (*31*), and most comets and Kuiper Belt objects formed further out, to ~35 AU. The plausibility of this scenario can be assessed by using the bulk compositions of these bodies together with knowledge of the CO snow line location. In particular, Kuiper Belt objects contain CO and the even more volatile N_2 (*32*, *33*), which implies that they must have formed beyond the CO snow line. Comets exhibit a range of CO abundances, some of which seem to be primordial, which suggests that the CO snow line was located in the outer part of their formation region of 15 to 35 AU (*34*). This is consistent with the CO snow line radius that we have determined in the TW Hya disk. However, in the context of the Nice model this CO snow line radius is too large for the ice giants and suggests that their observed carbon enrichment has a different origin than the accretion of CO ice (*30*). A caveat is that H_2O ice can trap CO, although this process is unlikely to be efficient enough to explain the observations. In either case, the CO snow line locations in solar nebula analogs such as TW Hya offer independent constraints on the early history of the solar system.

References and Notes

1. J. S. Lewis, *Science* **186**, 440–443 (1974).
2. D. J. Stevenson, J. I. Lunine, *Icarus* **75**, 146–155 (1988).
3. F. J. Ciesla, J. N. Cuzzi, *Icarus* **181**, 178–204 (2006).
4. A. Johansen *et al.*, *Nature* **448**, 1022–1025 (2007).
5. E. Chiang, A. N. Youdin, *Annu. Rev. Earth Planet. Sci.* **38**, 493–522 (2010).
6. B. Gundlach, S. Kilias, E. Beitz, J. Blum, *Icarus* **214**, 717–723 (2011).
7. K. Ros, A. Johansen, *Astron. Astrophys.* **552**, A137 (2013).
8. K. I. Öberg, R. Murray-Clay, E. A. Bergin, *Astrophys. J.* **743**, L16 (2011).
9. C. Hayashi, *Prog. Theor. Phys.* **70** (suppl.), 35–53 (1981).
10. E. Herbst, E. F. van Dishoeck, *Annu. Rev. Astron. Astrophys.* **47**, 427–480 (2009).
11. D. J. Wilner, P. D'Alessio, N. Calvet, M. J. Claussen, L. Hartmann, *Astrophys. J.* **626**, L109–L112 (2005).
12. S. E. Bisschop, H. J. Fraser, K. I. Öberg, E. F. van Dishoeck, S. Schlemmer, *Astron. Astrophys.* **449**, 1297–1309 (2006).
13. Y. Aikawa, E. Herbst, *Astron. Astrophys.* **351**, 233 (1999).
14. C. Qi *et al.*, *Astrophys. J.* **740**, 84 (2011).
15. C. Qi, K. I. Öberg, D. J. Wilner, *Astrophys. J.* **765**, 34 (2013).
16. E. A. Bergin, J. Alves, T. Huard, C. J. Lada, *Astrophys. J.* **570**, L101–L104 (2002).
17. J. K. Jørgensen, *Astron. Astrophys.* **424**, 589 (2004).
18. K. I. Öberg *et al.*, *Astrophys. J.* **734**, 98 (2011).
19. C. Walsh, H. Nomura, T. J. Millar, Y. Aikawa, *Astrophys. J.* **747**, 114 (2012).
20. Materials and methods are available as supplementary materials on *Science* Online.
21. J. H. Kastner, B. Zuckerman, D. A. Weintraub, T. Forveille, *Science* **277**, 67–71 (1997).
22. C. Qi, D. J. Wilner, Y. Aikawa, G. A. Blake, M. R. Hogerheijde, *Astrophys. J.* **681**, 1396–1407 (2008).
23. E. A. Bergin *et al.*, *Nature* **493**, 644–646 (2013).
24. S. M. Andrews *et al.*, *Astrophys. J.* **744**, 162 (2012).
25. K. A. Rosenfeld *et al.*, *Astrophys. J.* **757**, 129 (2012).
26. D. Hollenbach, M. J. Kaufman, E. A. Bergin, G. J. Melnick, *Astrophys. J.* **690**, 1497–1521 (2009).
27. K. Willacy, *Astrophys. J.* **660**, 441–460 (2007).
28. M. R. Hogerheijde, F. F. S. van der Tak, *Astron. Astrophys.* **362**, 697 (2000).
29. M. Lecar, M. Podolak, D. Sasselov, E. Chiang, *Astrophys. J.* **640**, 1115–1118 (2006).
30. S. E. Dodson-Robinson, K. Willacy, P. Bodenheimer, N. J. Turner, C. A. Beichman, *Icarus* **200**, 672–693 (2009).
31. K. Tsiganis, R. Gomes, A. Morbidelli, H. F. Levison, *Nature* **435**, 459–461 (2005).
32. T. C. Owen *et al.*, *Science* **261**, 745–748 (1993).
33. S. C. Tegler *et al.*, *Astrophys. J.* **751**, 76 (2012).
34. M. J. Mumma, S. B. Charnley, *Annu. Rev. Astron. Astrophys.* **49**, 471–524 (2011).

Acknowledgments: We are grateful to S. Schnee for data calibration and reduction assistance. C.Q. thanks the Smithsonian Astrophysical Observatory (SAO) Radio Telescope Data Center (RTDC) staff for their generous computational support. C.Q., K.I.O., and D.J.W. acknowledge grant NNX11AK63 from NASA Origins of Solar Systems. P.D. acknowledges a grant from Programa de Apoyo a Proyectos de Investigación e Innovación Tecnológica–UNAM. E.B. acknowledges support from NSF grant 1008800. This Report makes use of the following ALMA data: ADS JAO. ALMA#2011.0.00340.S. ALMA is a partnership of the European Southern Observatory (ESO) (representing its member states), NSF (USA), and the National Institute of Natural Sciences (Japan), together with the National Research Council (Canada) and the National Science Council and Academia Sinica's Institute of Astronomy and Astrophysics (ASIAA) (Taiwan), in cooperation with the Republic of Chile. The Joint ALMA Observatory is operated by ESO, Associated Universities, Inc. (AUI)/National Radio Astronomy Observatory, and the National Astronomical Observatory of Japan. We also make use of the Submillimeter Array (SMA) data: project #2004-214 (principal investigator, C.Q.). The SMA is a joint project between SAO and ASIAA and is funded by the Smithsonian Institution and the Academia Sinica.

Supplementary Materials

www.sciencemag.org/cgi/content/full/science.1239560/DC1
Materials and Methods
Figs. S1 to S5
Tables S1 to S3
References (*35*–*52*)

23 April 2013; accepted 2 July 2013
Published online 18 July 2013;
10.1126/science.1239560

A Quantum Many-Body Spin System in an Optical Lattice Clock

M. J. Martin,[1,2]*† M. Bishof,[1,2] M. D. Swallows,[1,2]‡ X. Zhang,[1,2] C. Benko,[1,2] J. von-Stecher,[1,2]§ A. V. Gorshkov,[3] A. M. Rey,[1,2]† Jun Ye[1,2]†

Strongly interacting quantum many-body systems arise in many areas of physics, but their complexity generally precludes exact solutions to their dynamics. We explored a strongly interacting two-level system formed by the clock states in ^{87}Sr as a laboratory for the study of quantum many-body effects. Our collective spin measurements reveal signatures of the development of many-body correlations during the dynamical evolution. We derived a many-body Hamiltonian that describes the experimental observation of atomic spin coherence decay, density-dependent frequency shifts, severely distorted lineshapes, and correlated spin noise. These investigations open the door to further explorations of quantum many-body effects and entanglement through use of highly coherent and precisely controlled optical lattice clocks.

Strongly correlated quantum many-body systems have become a major focus of modern science. Researchers are using quantum-degenerate atomic gases (*1*–*6*), ultracold polar molecules (*7*–*9*), and ensembles of trapped ions (*10*, *11*) to realize previously unidentified quantum phases of matter and simulate complex condensed matter systems. Another prom-

ising system is optical atomic clocks that use fermionic alkaline earth atoms. The most stable of these clocks now operate near the quantum noise limit (*12*), with an accuracy surpassing that of the cesium standard (*13*). With atom-light coherence times reaching several seconds, permitting optical spectral resolution well below 1 Hz (Fig. 1A), even very weak interactions (such as fractional energy level shifts of order $\geq 1 \times 10^{-16}$) can dominate the dynamics of these systems, and the corresponding complex spectrum can be probed precisely. Atomic interactions in optical lattice clocks were first studied in the context of density-dependent frequency shifts, which were attributed to *s*-wave collisions allowed by inhomogeneous excitation (*14*–*17*); *p*-wave interactions were assumed to be suppressed because of the ~1 μK sample temperature. More recently, in an optical clock based on ^{171}Yb atoms at ~10 μK, *p*-wave interactions were reported to lead to two-body losses and density shifts (*18*, *19*). At the same time, even at ~1 μK inelastic *p*-wave losses were observed in the ^{87}Sr system (*20*). The importance of many-body interactions in these clocks has been recognized theoretically (*15*–*17*), but measuring them experimentally has been challenging.

[1]JILA, National Institute of Standards and Technology and University of Colorado, Boulder, CO 80309, USA. [2]Department of Physics, University of Colorado, Boulder, CO 80309, USA. [3]Institute for Quantum Information and Matter (IQIM), California Institute of Technology, Pasadena, CA 91125, USA.

*Present address: California Institute of Technology, Pasadena, CA 91125, USA.

†Corresponding author. E-mail: ye@jila.colorado.edu (J.Y.); mjmartin@caltech.edu (M.J.M.); arey@jilau1.colorado.edu (A.M.R.)

‡Present address: AOSense, Sunnyvale, CA 94085, USA.

§Present address: Tech-X Corporation, Boulder, CO 80303, USA.

In this paper, we report the observation of quantum many-body effects in a high-density ^{87}Sr optical clock in a one-dimensional (1D) optical lattice. In a prior experiment (*21*), a strongly interacting regime (in which atom-laser and atom-atom interactions are energetically comparable) was reached by tightly confining the atoms in a 2D optical lattice, at the expense of reducing the occupancy to one or two atoms per site. In this work, we probed a strongly interacting system with an average of 20 atoms per disk-shaped 1D-lattice site and developed a detailed understanding of the complex many-body quantum dynamics. The role of *s*-wave collisions is suppressed by operating in the strongly interacting regime with highly homogeneous atom-laser coupling, making *p*-wave interactions, which operate collectively, dominant. The experimental observation of such quantum magnetic behavior at micro-Kelvin temperatures is made possible because the motional degrees of freedom are effectively frozen during the clock interrogation. Only the internal electronic degrees of freedom (pseudo-spin) are relevant, and these can be initialized in a pure state.

We considered an optical lattice clock that uses the $^1S_0 \rightarrow {}^3P_0$ (henceforth $|g\rangle \rightarrow |e\rangle$) clock transition in nuclear spin–polarized ^{87}Sr. It comprises an array of quasi-2D trap sites loaded with atoms at micro-Kelvin temperatures. The tight lattice confinement along the longitudinal direction Z freezes the dynamics and the population distribution across the trap sites. A single site populated with N atoms is modeled as a slightly anharmonic 2D oscillator with radial (longitudinal) frequency $\nu_R = 450$ Hz ($\nu_Z = 80$ kHz).

As shown in Fig. 1B, atoms within a given trap site can elastically interact with one another through the *p*-wave channel. Because all trap frequencies are much greater than the characteristic *p*-wave interaction energy, the motional degrees of freedom are effectively frozen, and interactions thus manifest themselves in the electronic $|g\rangle \leftrightarrow |e\rangle$ degrees of freedom that define our spin system (*22*). Fermi statistics guarantee that no two atoms within a given trap site occupy the same motional state. We initialized our nuclear spin–polarized gas with all atoms in the ground state $|g\rangle$, and this initial state can be expressed as a collective spin state with $S = N/2$, where $S(S+1)$ is the eigenvalue of the observable $\vec{S}\cdot\vec{S}$ and $\hat{S}^{\tau=x,y,z} = \sum_{j=1}^{N} \hat{S}_j^{\tau}$ are the collective spin operators. In the presence of the interatomic interactions and homogenous laser excitation, the collective nature of the system is maintained via two mechanisms. The first is the presence of a protective energy gap between collective spin manifolds (Fig. 1C), which prevents transitions away from the $S = N/2$ manifold (*22*). The second is the relatively small spread in mode-dependent interaction parameters with respect to the gap. Using the collective spin operators, we can thus describe the spin dynamics with the following Hamiltonian:

$$\hat{H}^{\mathrm{eff}}/\hbar = -\delta\hat{S}^z - \Omega\hat{S}^x + \chi(\hat{S}^z)^2 + C(N-1)\hat{S}^z + J^{\perp}\vec{S}\cdot\vec{S} + \mathcal{O}(S^z)^3 \quad (1)$$

where δ is the laser detuning from atomic resonance, Ω is the Rabi frequency of the driving laser, $\chi = (V_{gg} + V_{ee} - 2V_{eg})/2$, and $C = (V_{ee} - V_{gg})/2$. V_{gg}, V_{ee}, and V_{eg} represent *p*-wave interaction parameters between the three possible electronic symmetric states, $|gg\rangle$, $|ee\rangle$, and $\frac{1}{\sqrt{2}}(|ge\rangle + |eg\rangle)$ (Fig.

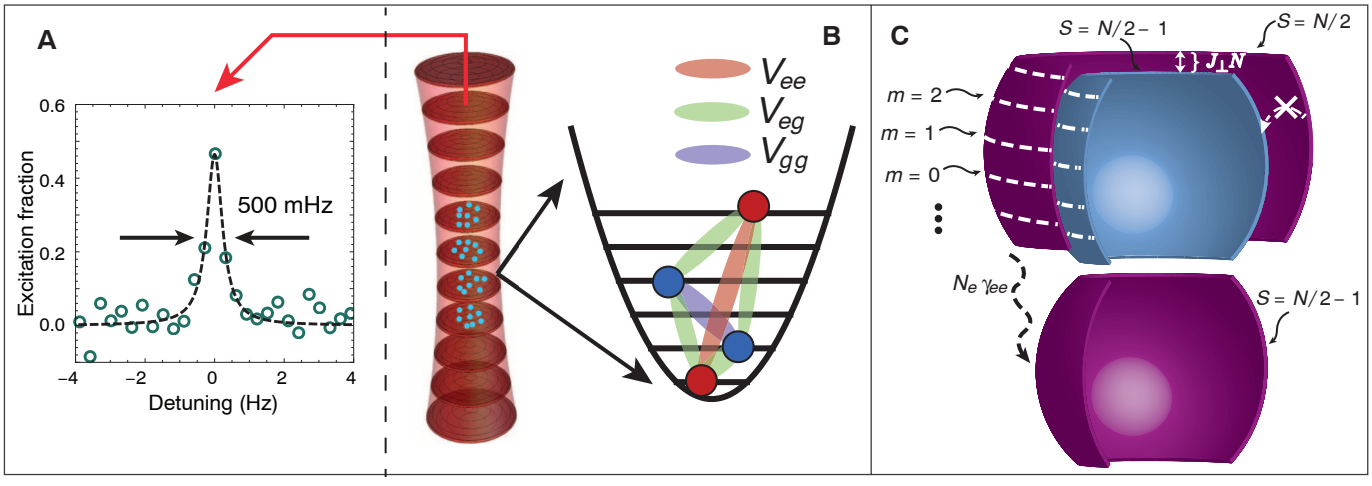

Fig. 1. Diagram of the interacting many-body system. (**A**) Spectroscopy of the ^{87}Sr clock transition in a 1D optical lattice, showing 500-mHz spectral resolution. The density is more than an order of magnitude lower than the typical operating condition. (**B**) Several hundred sites of the 1D vertical optical lattice are substantially occupied during the experiment. The average lattice occupancy is 20 atoms for the peak total atom number. Interactions between atoms are parametrized by the spin-dependent interaction parameters, $V_{gg} \propto b_{gg}^3$ (blue), $V_{eg} \propto b_{eg}^3$ (green), and $V_{ee} \propto b_{ee}^3$ (pink), with b^3 being the *p*-wave scattering volumes (*22*). (**C**) The many-body Hamiltonian has eigenstates comprising maximally symmetric superpositions (Dicke states, for which $S = N/2$) of electronic ground and excited states (purple shells). Slight inhomogeneities in the coupling strengths allow the maximally symmetric manifold to be coupled to the next lowest manifold with $S = N/2 - 1$ (nested blue shell), but this coupling is prevented by an energy gap resulting from the $J^{\perp}\vec{S}\cdot\vec{S}$ term in the Hamiltonian. Two-body inelastic losses connect maximally symmetric manifolds of $S \rightarrow S - 1$ and thus are not a strong decoherence mechanism.

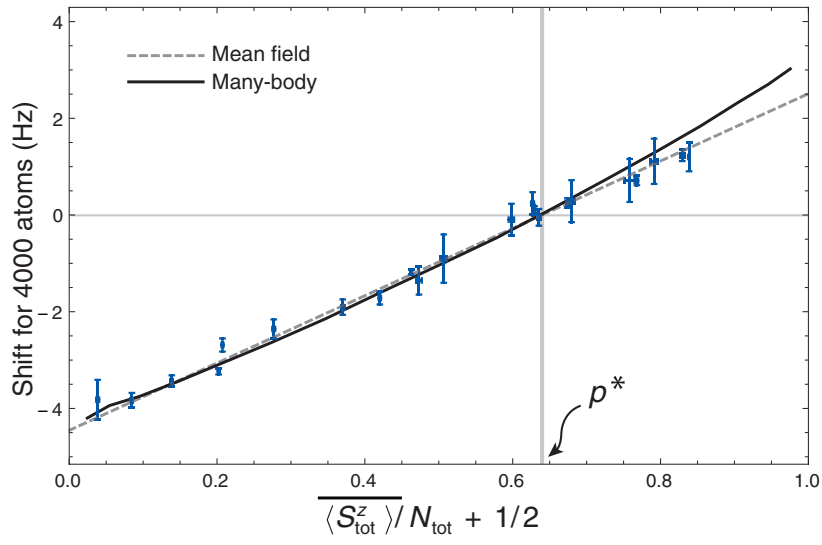

Fig. 2. Density shift in Ramsey spectroscopy fit with the full many-body solution. Because of the perturbative nature of this measurement, the mean-field approximation (dashed line) to the many-body theory agrees well with the data. The exact many-body solution in the absence of losses (solid curve) agrees best with the data only for lower values of total average spin $\langle \hat{S}^z_{tot} \rangle / N_{tot}$ because of the nonlinear $(\hat{S}^z)^3$ term in the Hamiltonian. The zero crossing occurs at an average excitation fraction, given by $\langle \hat{S}^z_{tot} \rangle / N_{tot} + 1/2$, of $p^* = 0.64(1)$. From the zero crossing and the measured slope, we extract χ and C.

1B). $J^{\perp}$ is responsible for the energy gap (*22*). We find that the weak modification of the motional degrees of freedom by interactions can be accounted for as a term of order $(S^z)^3$. Equation 1 links the spin dynamics of interacting thermal fermions at micro-Kelvin temperatures to those of two-mode Bose-Einstein condensates (BECs), and it has been shown both theoretically (*23*, *24*) and experimentally (*25*–*27*) to give rise to nontrivial many-body correlations and quantum noise–squeezed states. The validity of the collective model has been tested against the full multimode model with good agreement (*22*).

In the presence of excited-state inelastic loss, which has been observed in ^{87}Sr (*20*), our system becomes a many-body open quantum system. To capture the full many-body dynamics observed in the experiment, we solved a master equation in the presence of a two-body decay that is largely independent of the thermal occupation. The mode-independent losses preserved the collective nature of the system to leading order (Fig. 1C) and allowed us to solve the master equation efficiently for up to 50 atoms (*22*).

To determine the interaction parameters that characterize our spin Hamiltonian, Eq. 1, we mea-

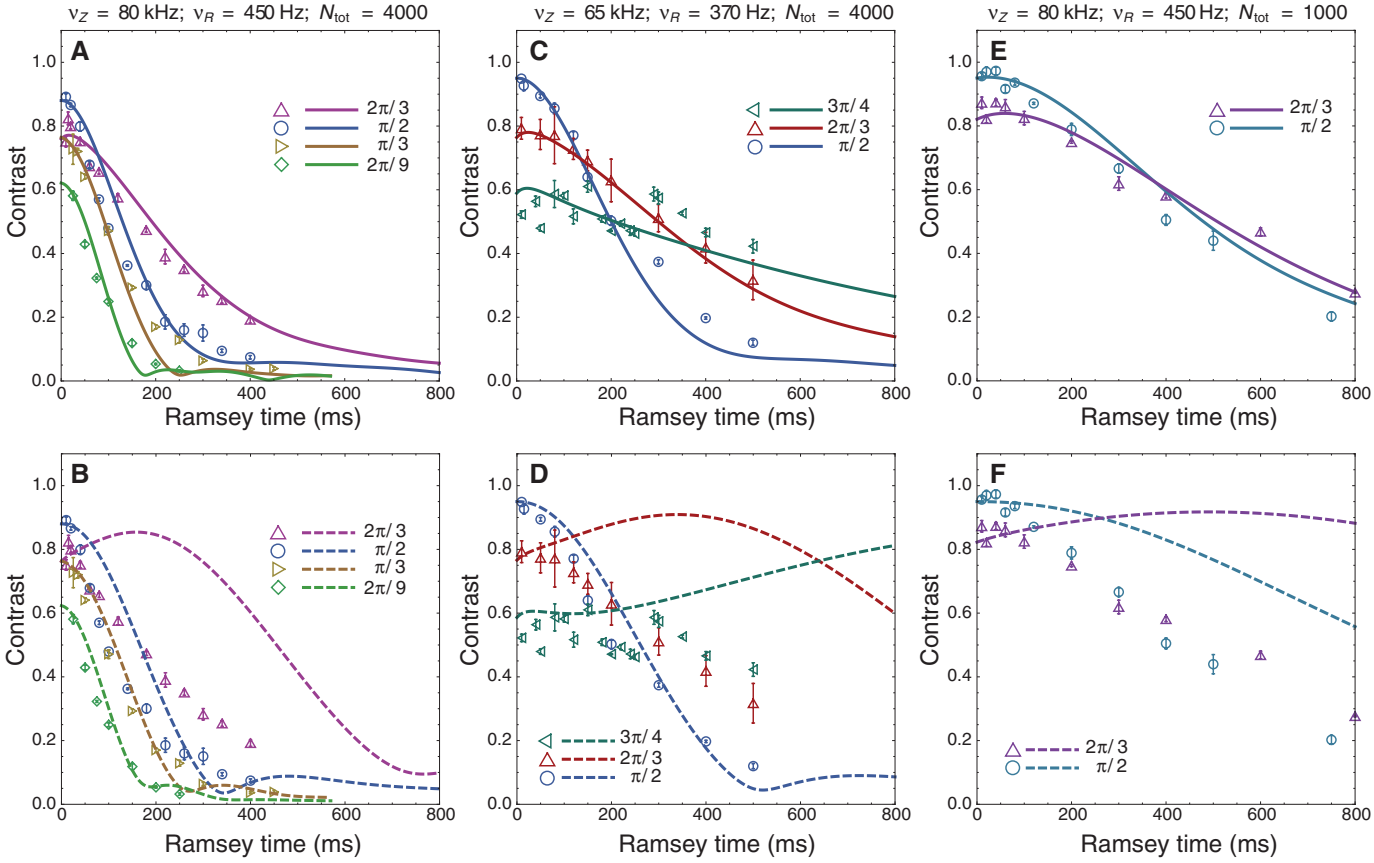

Fig. 3. Ramsey fringe contrast decay for varying initial pulse areas and experimental conditions. The pulse area values for the data and corresponding theory are given in the legends of the plots. Error bars represent the statistical error of each contrast measurement and thus do not account for systematic drifts that occur over the course of the experiment. The solid lines (top) are the many-body calculations, whereas the dashed lines (bottom) are using the mean-field approximation of the theory. The many-body model and the mean-field approximation agree in the limit of small initial pulse area (Bloch vector polar angle) but disagree for pulse areas $\gtrsim \pi/2$. This is an important confirmation of the dominance of many-body effects in this parameter regime. (**A** and **B**) ν_Z = 80 kHz, ν_R = 450 Hz, and N_{tot} = 4000; (**C** and **D**) ν_Z = 65 kHz, ν_R = 370 Hz, and N_{tot} = 4000; and (**E** and **F**) ν_Z = 80 kHz, ν_R = 450 Hz, and N_{tot} = 1000.

sured the density-dependent frequency shift of the clock transition using a modified Ramsey spectroscopy sequence. The initial pulse area $\theta_1 = \Omega T_R$, chosen so that $0 < \theta_1 < \pi$, controls the initial value of $\langle \hat{S}^z_{tot} \rangle$. Here, $\hat{S}^z_{tot}$ is the sum of $\hat{S}^z$ over the hundred relevant sites, so that $-N_{tot}/2 \leq \langle \hat{S}^z_{tot} \rangle \leq N_{tot}/2$, where N_{tot} is the total number of atoms loaded into the lattice. In the presence of two-body losses, $\langle \hat{S}^z_{tot} \rangle$ is not constant; thus, we used its time average, $\overline{\langle \hat{S}^z_{tot} \rangle}$, to compare with theory. We extracted $\overline{\langle \hat{S}^z_{tot} \rangle}$ from independent measurements periodically inserted into the clock sequence. The duration of the dark time, τ_{dark}, was fixed at 80 ms, and the final pulse area was set to $\pi/2$. We measured the shift by modulating the density by a factor of ~2 (Fig. 2).

Simple mean-field analysis of Eq. 1 (neglecting cubic terms and losses), in which the time-dependent operators are replaced by their expectation values, reveals that the average interaction experienced by a single atom behaves as an effective magnetic field along Z, $B(N) = NC + 2\chi\langle \hat{S}^z \rangle$, where $\langle \hat{S}^z \rangle = -(N/2)\cos\theta_1$. The mean-field density-dependent frequency shift $\Delta\nu(N) = B(N)/(2\pi)$ scales linearly with the excitation fraction and agrees with experimental observations (Fig. 2). Additionally, we fit an exact solution of Eq. 1 to the data. Both fits are shown in Fig. 2. To compare with the experiment, we always performed an average over the atom number distribution across the lattice sites. From this measurement, we extracted $\chi = 2\pi \times 0.20(4)$ Hz and $C = -0.3\chi$.

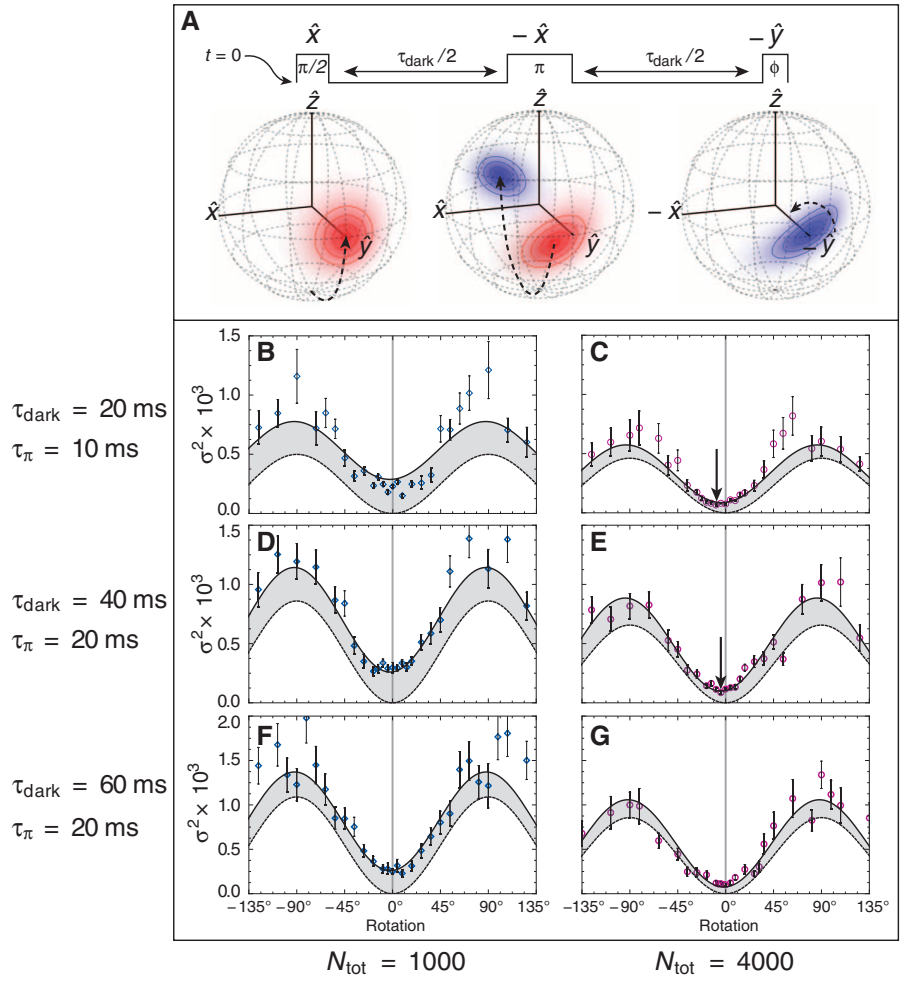

Fig. 4. Spin noise versus quadrature. (**A**) An initial pulse prepares a coherent state along $\hat{y}$, which then evolves for $\tau_{dark}/2$. An echo pulse then rotates the many-body state 180° about $-\hat{x}$. After an additional evolution time of $\tau_{dark}/2$, a final pulse rotates the state about $-\hat{y}$, and the spin noise is measured. The π-pulse has duration τ_π. The many-body state depicted here represents the spin evolution of a 20-atom ensemble in a single trap site, with τ_{dark} = 40 ms. To remove spurious effects due to slow drifts in atom number, the data are processed as detailed in (*22*) in order to remove the potential bias. For (**B** to **G**), the dashed line is the pure laser noise extracted from a fit to the data. The solid line is the laser noise plus the full many-body prediction of the spin noise. This full theory is simultaneously fit to both the low– and high–atom-number curves so as to extract the laser noise for a given dark time. Vertical arrows indicate significantly phase-shifted minima in the experimentally measured spin noise, which is consistent with the predictions of the many-body theory. π-pulse times and τ_{dark} values are indicated at left, and total atom number is indicated at bottom.

As a further step, we directly measured the spectrum of the many-body Hamiltonian with subherz spectral resolution and as a function of the drive strength, parameterized by the Rabi frequency Ω. We found that for $\Omega >> N\chi$, the lineshapes are perturbatively shifted. However, for $\Omega \lesssim N\chi$, the lineshapes become significantly distorted, and the onset of an interaction blockade mechanism is observed, reflecting the dominant effect of strong interactions on the many-body spectrum. The observed Rabi lineshapes can be fully reproduced with the mean-field treatment by using the interaction parameters extracted from the density shift measurements. In this case, a full many-body treatment of the master equation agrees with the mean-field predictions.

To explore the development of many-body correlations during the full many-body dynamical evolution, we measured the Ramsey fringe contrast, which can undergo a periodic series of collapses and revivals, reflecting the quantized structure of the many-body spectrum. The results require a beyond–mean-field treatment. The mean-field model at the single-site level (with fixed N) predicts no decay of the Ramsey fringe contrast because when correlations are neglected, the interactions lead only to a pure precession of the collective Bloch vector (*22*). By taking the average over atom distributions among lattice sites and properly treating two-body loss during the Ramsey dark time, the mean-field model does show a decay of the contrast. However, this decay is associated mainly with dephasing arising from different precession rates exhibited by sites with different N.

For the Ramsey sequence designed to measure the fringe contrast effects, the pulse durations are <6 ms, satisfying $\Omega >> N\chi$, to suppress interaction effects during the pulses. We applied the final $\pi/2$ readout pulse with a variable relative optical phase of 0° to 360° and recorded the fraction of excited atoms as a function of the readout phase. The contrast of the resulting fringe was extracted in a manner that was insensitive to the frequency noise of the ultrastable clock laser (*22*).

We explored three distinct experimental conditions in order to rule out single-particle decoherence mechanisms and thoroughly test the model. The first condition represents the typical operating parameters of the lattice clock, with $N_{tot} = 4 \times 10^3$ and $\nu_Z = 80$ kHz. In the second case, we reduced the lattice intensity so that $\nu_Z =$ 65 kHz, which results in a reduction of the density by a factor of ~1.8. Last, we maintained $\nu_Z = 80$ kHz but reduced the atom number to $N_{tot} = 1 \times 10^3$. Under all conditions, the full many-body density matrix model reproduces the experimental observations well (Fig. 3, A, C, and E). The inclusion of the $\langle \hat{S}^z \rangle^3$ correction improves the theory-experiment agreement, especially for pulse areas $\theta_1 > \pi/2$ and for the high-density conditions (*22*). We also observed a striking breakdown of the mean-field model for $\theta_1 \gtrsim \pi/2$, where many-body corrections are dominant (Fig. 3, B, D, and F).

The frequency shift, lineshape, and Ramsey fringe contrast are quantities that all depend on the first-order expectation values of the spin operators $\langle \hat{S}^{x,y,z} \rangle$. We next turned our attention to the distribution of quantum noise, which depends on the second-order moments of the spin operators, such as $\langle (\hat{S}^x)^2 \rangle - \langle \hat{S}^x \rangle^2$ and $\langle \hat{S}^x \hat{S}^z + \hat{S}^z \hat{S}^x \rangle - 2 \langle \hat{S}^x \rangle \langle \hat{S}^z \rangle$. Given that the form of the Hamiltonian in Eq. 1 is known to produce squeezed and entangled states (*23*), the distribution of the spin noise becomes a compelling measurement to probe many-body correlations beyond the mean field.

To minimize single-particle dephasing effects (for example, arising from the distribution of site occupancies), we added a spin-echo pulse to the Ramsey sequence. As a result, the sensitivity to low-frequency laser noise was reduced at the expense of increased sensitivity to high-frequency laser noise. With atoms initialized in $|g\rangle$, we followed the pulse sequence (Fig. 4) so as to manipulate and measure the spin noise of the many-body state. For each value of the final rotation angle, representing a specific quadrature in which we measured the spin noise, we repeatedly recorded $\langle \hat{S}^z_{\mathrm{tot}} \rangle / N_{\mathrm{tot}}$ via measurements of the final atomic excitation fraction after the Ramsey sequence. From the data, we determined $\sigma \equiv \langle (\hat{S}^z_{\mathrm{tot}})^2 \rangle / N^2_{\mathrm{tot}} - \langle \hat{S}^z_{\mathrm{tot}} \rangle^2 / N^2_{\mathrm{tot}}$ by analyzing the pair variance for successive measurement of $\langle \hat{S}^z_{\mathrm{tot}} \rangle / N_{\mathrm{tot}}$. The quantum limit of σ^2 is important for defining the ultimate stability of lattice clocks (*12*). For an ideal coherent spin state of the entire ensemble, the standard quantum limit (SQL) of σ^2 is given by $\sigma^2_{\mathrm{sql}} = p(1-p)/N_{\mathrm{tot}}$, where p is the probability of finding an atom in the excited state and can be estimated as $p = \langle \hat{S}^z \rangle / N_{\mathrm{tot}} + 1/2$.

We performed measurements for different N_{tot} and τ_{dark}—the total atom number and Ramsey free evolution time, respectively—in order to probe the time evolution of the spin noise distribution. Long π pulses were used to reduce the sensitivity to spurious high-frequency components of laser noise. For $N_{\mathrm{tot}} = 1 \times 10^3$, the quantum noise contribution to the spin noise is comparable with that of the laser noise (Fig. 4); however, with $N_{\mathrm{tot}} = 4 \times 10^3$ the laser noise is responsible for a larger fraction of the noise in repeated measurements of $\langle \hat{S}^z \rangle$.

There are qualitative differences between the low– and high–atom-number cases; for example, for $N_{\mathrm{tot}} = 4 \times 10^3$ with $\tau_{\mathrm{dark}} = 20$ and 40 ms we observed a phase shift for the minimum of the spin noise. To compare the predictions of the full many-body master equation with the experiment, we added the effect of laser noise in quadrature with the calculated spin quantum noise. In the absence of laser noise, the theory predicts a small degree of sub-SQL squeezing. This effect is masked by laser noise in both the theoretical prediction for the total spin noise and in our experimental observations but gives rise to a shift of the spin noise minimum with respect to measurement quadrature. We additionally treated the effects of interactions during the laser pulses. The theory predicts the direction and magnitude of the phase shift of the noise minimum in agreement with the experimental observations (Fig. 4), in addition to significantly enhanced spin noise for rotations near ±90°. Despite the presence of laser noise, the measurements of the total spin noise are consistent with the many-body spin model.

Although the investigation described here is restricted to nuclear-spin–polarized gases, exploration of similar many-body effects in a clock making use of additional nuclear spin degrees of freedom with SU(N) symmetry may allow investigation of unconventional frustrated quantum magnetism (*28*–*30*).

References and Notes

1. M. Greiner, O. Mandel, T. Esslinger, T. W. Hänsch, I. Bloch, *Nature* **415**, 39–44 (2002).
2. I. Bloch, W. Zwerger, *Rev. Mod. Phys.* **80**, 885–964 (2008).
3. Y.-J. Lin, R. L. Compton, K. Jiménez-García, J. V. Porto, I. B. Spielman, *Nature* **462**, 628–632 (2009).
4. G. B. Jo *et al*., *Science* **325**, 1521–1524 (2009).
5. S. Will *et al*., *Nature* **465**, 197–201 (2010).
6. J. Simon *et al*., *Nature* **472**, 307–312 (2011).
7. K. K. Ni *et al*., *Science* **322**, 231–235 (2008).
8. M. H. G. de Miranda *et al*., *Nat. Phys.* **7**, 502–507 (2011).
9. A. Chotia *et al*., *Phys. Rev. Lett.* **108**, 080405 (2012).
10. K. Kim *et al*., *Nature* **465**, 590–593 (2010).
11. J. W. Britton *et al*., *Nature* **484**, 489–492 (2012).
12. T. L. Nicholson *et al*., *Phys. Rev. Lett.* **109**, 230801 (2012).
13. A. D. Ludlow *et al*., *Science* **319**, 1805–1808 (2008).
14. G. K. Campbell *et al*., *Science* **324**, 360–363 (2009).
15. A. M. Rey, A. V. Gorshkov, C. Rubbo, *Phys. Rev. Lett.* **103**, 260402 (2009).
16. K. Gibble, *Phys. Rev. Lett.* **103**, 113202 (2009).
17. Z. H. Yu, C. J. Pethick, *Phys. Rev. Lett.* **104**, 010801 (2010).
18. N. D. Lemke *et al*., *Phys. Rev. Lett.* **107**, 103902 (2011).
19. A. Ludlow *et al*., *Phys. Rev. A* **84**, 052724 (2011).
20. M. Bishof *et al*., *Phys. Rev. A* **84**, 052716 (2011).
21. M. D. Swallows *et al*., *Science* **331**, 1043–1046 (2011).
22. Materials and methods are available as supplementary materials on *Science* Online.
23. A. Sørensen, L. M. Duan, J. I. Cirac, P. Zoller, *Nature* **409**, 63–66 (2001).
24. M. Kitagawa, M. Ueda, *Phys. Rev. A* **47**, 5138–5143 (1993).
25. J. Estève, C. Gross, A. Weller, S. Giovanazzi, M. K. Oberthaler, *Nature* **455**, 1216–1219 (2008).
26. C. Gross, T. Zibold, E. Nicklas, J. Estève, M. K. Oberthaler, *Nature* **464**, 1165–1169 (2010).
27. B. Lücke *et al*., *Science* **334**, 773–776 (2011).
28. A. V. Gorshkov *et al*., *Nat. Phys.* **6**, 289–295 (2010).
29. C. Wu, J.-P. Hu, S.-C. Zhang, *Phys. Rev. Lett.* **91**, 186402 (2003).
30. M. A. Cazalilla, A. F. Ho, M. Ueda, *New J. Phys.* **11**, 103033 (2009).

Acknowledgments: We thank S. Blatt, J. Thomsen, W. Zhang, T. Nicholson, J. Williams, B. Bloom, and S. Campbell for technical help and A. D. Ludlow, K. R. A. Hazzard, M. Foss-Feig, A. J. Daley, and J. K. Thompson for discussions. The work is supported by the National Institute of Standards and Technology, Defense Advanced Research Projects Agency Optical Lattice Emulator Program administered by Army Research Office, NSF, and Air Force Office of Scientific Research. M.B. acknowledges support from the National Defense Science and Engineering Graduate fellowship program. A.V.G. acknowledges support from NSF IQIM, the Lee A. DuBridge Foundation, and the Gordon and Betty Moore Foundation.

Supplementary Materials

www.sciencemag.org/cgi/content/full/341/6146/632/DC1
Materials and Methods
Supplementary Text
Figs. S1 to S5
References (*31*–*44*)

22 February 2013; accepted 1 July 2013
10.1126/science.1236929

Writing and Deleting Single Magnetic Skyrmions

Niklas Romming, Christian Hanneken, Matthias Menzel, Jessica E. Bickel,* Boris Wolter, Kirsten von Bergmann,† André Kubetzka,† Roland Wiesendanger

Topologically nontrivial spin textures have recently been investigated for spintronic applications. Here, we report on an ultrathin magnetic film in which individual skyrmions can be written and deleted in a controlled fashion with local spin-polarized currents from a scanning tunneling microscope. An external magnetic field is used to tune the energy landscape, and the temperature is adjusted to prevent thermally activated switching between topologically distinct states. Switching rate and direction can then be controlled by the parameters used for current injection. The creation and annihilation of individual magnetic skyrmions demonstrates the potential for topological charge in future information-storage concepts.

Magnetic skyrmions (*1*) are topologically stable, particle-like spin configurations that carry a characteristic topological charge S, which is essentially a measure of the magnetization curvature. For a surface area A, S is defined as $S = \frac{1}{4\pi} \int_A \mathbf{n} \cdot \left(\frac{\partial \mathbf{n}}{\partial x} \times \frac{\partial \mathbf{n}}{\partial y} \right) dx dy$, where $\mathbf{n}$ is the normalized magnetization vector and x and y are the spatial coordinates. A single skyrmion carries a quantized charge of $S = +1$; for an antiskyrmion, the charge is $S = -1$. In contrast, a spin spiral and the ferromagnetic (FM)

Institute of Applied Physics, University of Hamburg, D-20355 Hamburg, Germany.

*Present address: Department of Physics, Mount Holyoke College, 50 College Street, South Hadley, MA 01075, USA.
†Corresponding author. E-mail: kubetzka@physnet.uni-hamburg.de (A.K.); kbergman@physnet.uni-hamburg.de (K.v.B.)

A Quantum Many-Body Spin System in an Optical Lattice Clock

M. J. Martin, M. Bishof, M. D. Swallows, X. Zhang, C. Benko, J. von-Stecher, A. V. Gorshkov, A. M. Rey, and Jun Ye

Science, 341 (6146), • DOI: 10.1126/science.1236929

Strongly Correlated Clocks

Optical lattice clocks with alkaline earth atoms provide one of the most stable time-keeping systems. Such clocks, in general, exhibit shifts in their transition frequencies as a consequence of interactions between atoms. Can this sensitivity be used to explore the dynamics of strongly correlated quantum systems? Martin *et al.* (p. 632) used a 1-dimensional optical lattice clock to study quantum many-body effects. Whereas the clock shift itself could be modeled within the mean field approximation, quantities such as spin noise required a full many-body treatment. This system may be useful for the quantum simulation of exotic magnetism.